Enhanced 3D Myocardial Strain Estimation from Multi-View 2D CMR Imaging

Mohamed Abdelkhalek[1, 3], Heba Aguib[1, 3], Mohamed Moustafa[2], Khalil ElKhodary [1]

Mechanical Engineering Department, The American University in Cairo, Cairo 11835, Egypt.[1]

Computer Science Department, The American University in Cairo, Cairo, 11835 Egypt[2]

Biomedical Engineering & Innovation Lab, Aswan Heart Centre, Aswan, 81511, Egypt[3]

Correspondence should be addressed to Mohamed Abdelkhalek; mohamed-abdelkhalek@aucegypt.edu

Abstract

In this paper, we propose an enhanced 3D myocardial strain estimation procedure, which combines complementary displacement information from multiple orientations of a single imaging modality (untagged CMR SSFP images). To estimate myocardial strain across the left ventricle, we register the sets of short-axis, four-chamber and two-chamber views via a 2D non-rigid registration algorithm implemented in a commercial software (Segment, Medviso). We then create a series of interpolating functions for the three orthogonal directions of motion and use them to deform a tetrahedral mesh representation of a patient-specific left ventricle. Additionally, we correct for overestimation of displacement by introducing a weighting scheme that is based on displacement along the long axis. The procedure was evaluated on the STACOM 2011 dataset containing CMR SSFP images for 16 healthy volunteers. We show increased accuracy in estimating the three strain components (radial, circumferential, longitudinal) compared to reported results in the challenge, for the imaging modality of interest (SSFP). Our peak strain estimates are also significantly closer to reported measurements from studies of a larger cohort in the literature. Our proposed procedure provides a fast way to accurately reconstruct a deforming patient-specific model of the left ventricle using the commonest imaging modality routinely administered in clinical settings, without requiring additional or specialized imaging protocols.

Keywords

Patient-specific, Cardiac Magnetic Resonance, Left Ventricle, Motion Tracking, Strain Analysis

Introduction

When we consider the multiplicity of mechanisms that underly the dynamics of a beating heart, such as the governing chemical, electrical, structural and fluidic processes, a need for sophisticated computational models becomes clear. Such models are typically designed to study only some aspect of a heart-beat, from the phenomena exhibited by blood flow within the chambers (De Santis et al., 2018), to the electro-mechanics of the myocardium (Baillargeon et al., 2014), to the evolving geometry and shape of the ventricular walls (Medvedofsky et al., 2018), to the associated deformation patterns of the ventricles (Tobon-Gomez et al., 2013). Of general interest to such modelling efforts, is the translation of these governing principles to a computational domain, that is sufficiently representative of conditions in actual patients. This is necessary for the resulting models to be of clinical value and possibly assist in individualized therapy (Gray and Pathmanathan, 2018). In particular, a study of the kinematics and deformation of the left ventricle (LV) on a patient-specific level is an example of computational modelling that has of recent gained traction in clinical research (Gray and Pathmanathan, 2018). It can be divided into two approaches: tracking and analysis. Tracking falls within the fields of image processing and computer vision, since the underlying raw data that one starts with comes from a set of clinically acquired images in different modalities (Ginat et al., 2011). Some correspondence (image registration) then needs to be established between the images acquired at different times for a given region of interest (ROI) (Rueckert and Aljabar, 2010). On the other hand, analysis includes methods from computational geometry and computational mechanics (Amini and Prince, 2001; Wang and Amini, 2012). Quantities of clinical import that can be identified, and calculated for the LV, via both these approaches, include global metrics, such as chamber volume, wall thickness. And regional metrics, such as local displacement, strain and curvature (Fig. 1).

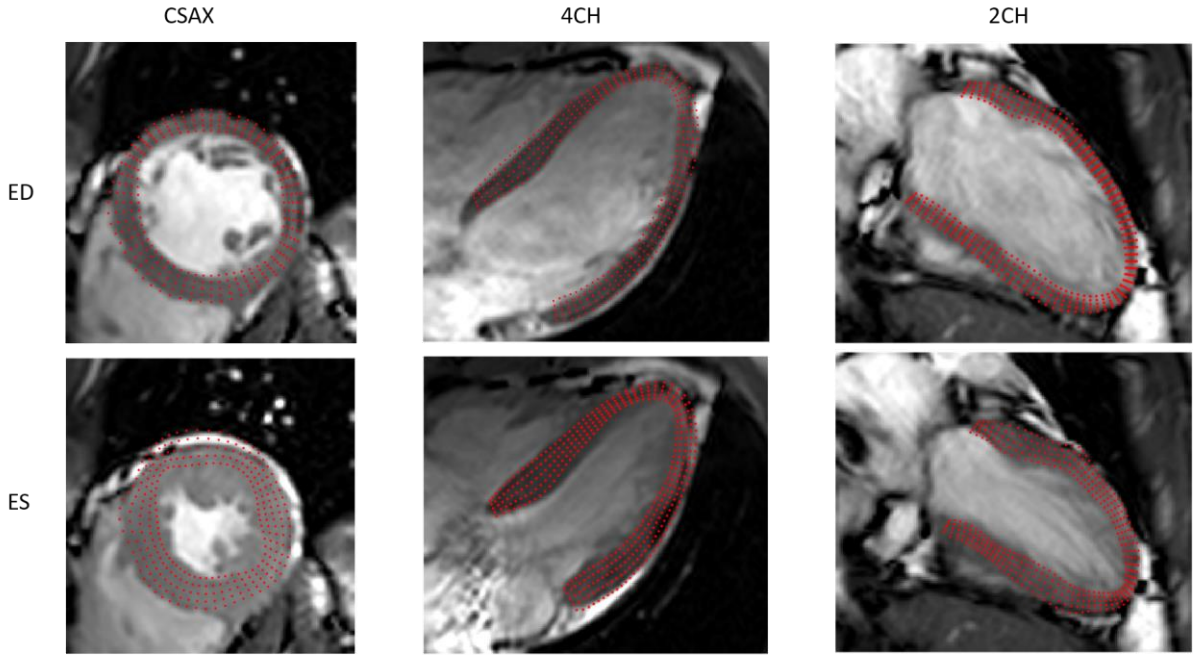

Figure 1. CMR SSFP images of the left ventricle in the different views at end-diastole ED and end-systole ES. Red points indicated tracked myocardium points using 2D registration method employed in Segment Medviso.

Strategies and methods are varied in terms of the choice of image acquisition, transformation modelling, similarity metrics, and post-registration error correction (Amini and Prince, 2001; Rueckert and Aljabar, 2010). Historically, for instance, LV motion tracking was employed by direct methods of motion analysis within the frequency domain of the images (Tobon-Gomez et al., 2013; Wang and Amini, 2012). Recently, there has been renewed clinical interest in LV motion tracking on untagged Cardiovascular Magnetic Resonance (CMR) images to help overcome the fading of tags over a cardiac cycle (Hergan et al., 2008). Moreover, interest in approaches that combine information from multiple imaging sources (multi-modality) has also grown (Werys et al., 2015). In tandem, non-rigid registration methods that deal with cardiac deformation have also been widely adopted. These registration methods focus on elastic and optical flow methods that do not in general allow for motion tracking within the myocardium, but only along its borders (Hergan et al., 2008; Heyde et al., 2013). Elastic methods seem preferable, however, since they add a smoothing penalty to the cost function in their optimization scheme, inspired by the bending energy of thin sheets of metal (Morais et al., 2013). Furthermore, a temporal smoothing strategy could be introduced (Morais et al., 2017). Their higher accuracy in comparison with other methods, e.g. optical flow, has thus been argued (Heyde et al., 2013; Morais et al., 2017, 2013). There are several examples of non-rigid registration methods in the literature. For instance, Fraunhofer MEVIS developed an approach based on a frequency domain analysis of 3DTag and 3D ultrasound (3DUS) images. They employ 2D estimates of displacement fields, slice-wise, in different orientations, and combine the resultant displacement fields into the 3D domain. No temporal consistency constraint is enforced (Tobon-Gomez et al., 2013). Imperial College London – University College London (IUCL) employ a combined 3D free-form deformation (FFD) registration scheme that uses 3DTag and steady-state free precession (SSFP) images. Their approach is primarily designed for MR sequences, with a spatially varying weighting scheme to decide on the influence of displacements between the 3DTag and SSFP sequences (Duckett et al., 2012; Tobon-Gomez et al., 2013). Their approach has the known limitation that circumferential and longitudinal motion are underestimated in the SSFP images, and that the tracking of myocardium contours is rather difficult in 3DTag images, due to tag-fading at peak systole. Conversely, Universitat Pompeu Fabra (UPF) employs a time modified FFD (TFFD) approach by including time in their registration process, to introduce their optimization over velocity instead of displacement, which improves the process by enforcing temporal coherence in the displacement of points along the cardiac cycle (Tobon-Gomez et al., 2013). Also, incompressibility of the myocardium (i.e. volume conservation) is included as a regularization term in their optimization. As a last example, the Inria-Asclepios project also employs a velocity field-based registration scheme but using a non-parametric approach (i.e. no spline control grid) with the iLogDemons algorithm (Tobon-Gomez et al., 2013). They also introduce incompressibility of the myocardium as a smoothing term in the optimization and were able to apply the algorithm on all image types. All these discussed approaches, except MEVIS, used a 3D registration scheme. MEVIS combine the more classical frequency domain two-dimensional analysis with 3D reconstruction at later stage. Also, all approaches exhibited rather expensive computational times, exceeding hours in execution per case. Except for IUCL and MEVIS, a manual segmentation step is required in image pre-processing (Tobon-Gomez et al., 2013). Also, as all approaches focused on assessing motion tracking, they do not elaborate on the pre-requirement of obtaining a geometrical representation of the LV and instead relied on the ground truth meshes provided by the benchmark challenge which was obtained by manually deforming a template LV mesh acquired from CT image scans (Tobon-Gomez et al., 2013), which for the purposes of this framework we included our own mesh reconstruction step from SAX images as it corresponds to real life clinical settings where a template mesh may not be available, this also helps in creating LV shapes as close to real morphologies as possible. As a final remark,

to the best of our knowledge Segment Medviso is one of the few FDA approved myocardial strain analysis commercial software that works on untagged CMR images without requiring special processing of images, beyond those routinely administered for LV function assessment (Morais et al., 2017; Schulz-Menger et al., 2020). Hence, the motivation was to complement the software's clinical workflow with a) 3D strain interpolation and b) patient specific 3D mesh model of the LV, based on manual contouring of LV borders from CMR images.

Materials and Methods

We begin by defining our problem as follows. We are given a sequence of images representing the heart over time, where 30 frames span about 1s of cardiac motion, imaging it as it contracts to eject blood, and then relaxes to refill, i.e. one cardiac cycle. The main image stack is of the short axis (SAX), which represents a top view of the heart chambers, and is composed of multiple 2D slices that trace the entirety of the LV from base to apex. Additionally, we have 2D image stacks of two- and four-chamber views that are orthogonal to the short axis (Fig. 1). The ROIs associated with the LV are three regions: the outer layer (epicardium), the inner layer (endocardium) and the volume between them (myocardium), which appear in 2D MRI images as per (Fig. 2A). After assembling the image stack and loading them in a commercial software (Segment) we proceed to manually segment the ROIs for the first timeframe, which should always correspond to the maximal LV volume, known as the end-diastolic stage (ED). We then start the tracking process which follows the segmented ROI as it deforms over the cardiac cycle. We export the results of segmentation and tracking for coding on MATLAB and proceed to transform the tracked points into physical space, aligning the different views and up sampling their point clouds by means of spline interpolants (Video. 1). Next, we interpolate 3D displacement fields that combine motion data from the different views and reconstruct the surface and volume meshes from ED segmentation. This allows us to deform the new tetrahedral mesh representations of the LV (Video. 1), allowing for the calculation of strain distribution using finite element approximations on the deformation of each mesh element.

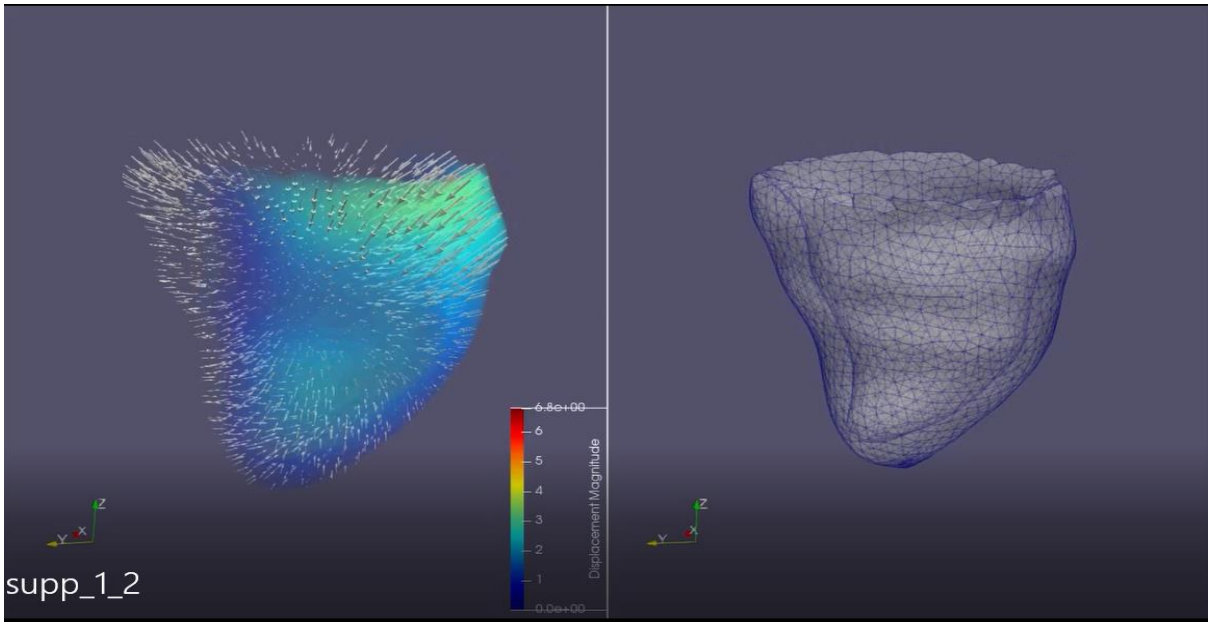

Video. 1 Animation of original tracked points from software and then, of final interpolated mesh as it deforms due to influence of combined displacement from the multiple views.

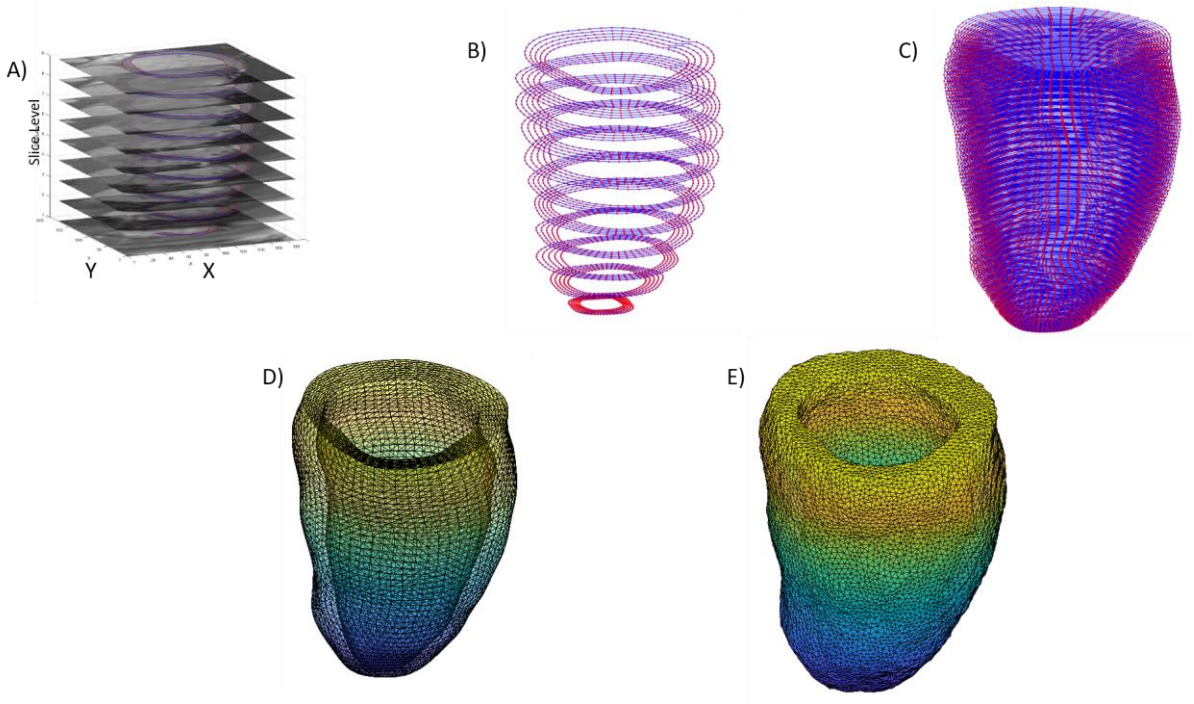

Figure 2. Overview of meshing pipeline in our proposed method. A) Initial manual segmentation of myocardium from images at end-diastole. B) Initial point cloud of tracked points from Segment. C) Up sampled and refined point cloud. D) Initial surface reconstruction. E) Final volumetric mesh of myocardium.

Segmentation

All pre-processing, which involves a consideration of DICOM metadata headers (Ginat et al., 2011) and manual segmentation, was performed on Segment. After loading and assembling the image stacks in the software, the next step is to manually segment the endo- and epicardial walls of the LV on the images using a graphical user interface tool provided by the same software (Fig. 1, Fig. 2A). This is a critical step that requires anatomical knowledge of the 3D morphology of the LV, its projections, and may be affected by image artefacts, noisy acquisitions, as well as observer experience. In our research we closely followed the segmentation guidelines recommended by the Task Force for Post Processing of the Society for Cardiovascular MR (SCMR) (Schulz-Menger et al., 2020). In Fig. 2A we show the process of contouring/segmentation of myocardial borders in the different slice levels.

Registration

Next, a tracking algorithm employed by the Segment Strain Analysis Module is used to estimate myocardial point displacements by using a non-rigid image registration method that has the following components. A transformation function using the B-Spline product transform, where control point displacements are estimated by an optimization scheme that minimizes an image similarity metric between pairs of consecutive images in the sequence (Morais et al., 2017, 2013). Additionally, a regularization term that penalizes rough deformations is used in the optimization scheme. The similarity metric is treated simply as the sum of square differences SSD (Morais et al., 2013) between two consecutive image frames and the regularization term is based on the bending energy which can be derived from second-order derivatives of the cost function (Schwarz, 2007). An important addition to this registration scheme, unlike other approaches, is its incorporation of time as an independent variable in the optimization process, which helps eliminate jagged or unphysical motion trajectories that are induced by treating inter-frame registrations independently (Morais et al., 2013). This process is repeated for each view and for each 2D image in the stack.

We next extract scattered displacement fields from the resultant tracked points by subtracting from the new positions at each frame (Fig. 3B) the original positions in the reference frame at ED (Fig. 3A). An important implication of the FFD approach employed by Segment is that we can also follow myocardial point displacements inside the tracked boundaries, unlike approaches based on optical flow methods (Hergan et al., 2008). The general form of a non-rigid elastic registration method based on FFD can be summarized as in (Heyde et al., 2013; Schwarz, 2007) in (Eq. 1, 2, 3) as

$$C = S(\varphi) + \alpha R(\varphi) \qquad (1)$$

$$S(\varphi) = \frac{1}{M}\sum_{i=0}^{M}\left(I_f(x) - I_m\big(T(x,\varphi)\big)\right)^2 \qquad (2)$$

$$T(x) = x + u(x) \qquad (3)$$

Where C is the cost function and S is the similarity measure (sum of square differences) between a fixed image I_f and a moving image I_m after applying a transformation T, which is defined as a displacement of some pixel/voxel located at x defined by a deformation field φ.

The R term is the cost function that relates to smoothing/regularization with α . The objective of the optimization is to find the optimal parameters of T that minimize (Eq. 1). The choice of R, T, and (x), as well as the strategy of obtaining the similarity measure S, are what determine the non-rigid registration algorithm. In this work, we complement the 2D tracking results provided by Segment Strain Analysis module which was used as is, detailed algorithm implementation details can be reviewed in (Heyde et al., 2013; Morais et al., 2017, 2013).

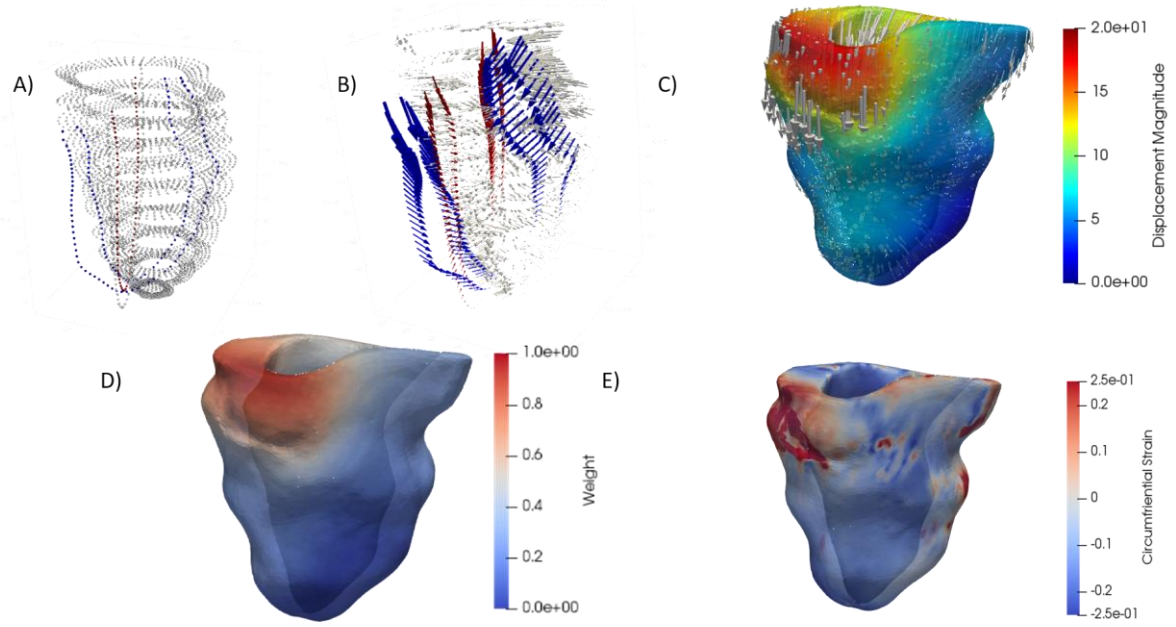

Figure 3. Overview of displacement interpolation and strain calculation pipeline in our proposed method. A) Initial aligned point cloud representation of left ventricle segmentations. B) Displacement vectors from 2D registration at peak-systole C) Left ventricle tetrahedral mesh with color coded displacement field and displacement vectors at each point with length of vectors representing magnitude of displacement. D) Mesh with color coded weight map for each point representing degree of influence of displacement from each view. E) Mesh with color coded strain map of circumferential strain.

Point Cloud Construction and Alignment

Upon exporting to MATLAB the sorted images, segmentation and tracking information, we need to perform a series of coordinate transformations that serve the dual purpose of aligning the different views which define the ROI, and facilitating the interpolation/extrapolation of the 3D displacement fields within a common coordinate system. This is accomplished by relying on the DICOM metadata information in each image stack, which provides the required information, i.e. position, orientation, scale and size, to allow a transformation of the images, segmentation and tracked points to the RL-AP-FH anatomical space (Ginat et al., 2011). We can then transform the resultant datasets to a global Cartesian coordinate system centred at the LV's centre of mass defined by averaging the nodal positions in the first time frame, with the major axes of the ROI aligned with X, Y, Z unit vectors respectively (Fig. 2B). The spatial resolution of the scattered points that are retrieved from segmentation, and their associated displacement fields, is in general deemed insufficient to fully reconstruct the LV, or to properly interpolate its displacement fields. Hence, we up-sample the point clouds, relying on natural cubic splines (Ginnis et al., 2017; Lee, 1989) to construct spline cages that follow the ordered set of points that cover the ROI in its different spatial views (Fig. 2C). By stitching/joining

endo and epi contours and then up-sampling points along these splines, we can generate higher quality point cloud representations of the LV (Fig. 4), with the added ability to refine and smoothen our representation as needed, by means of predefined user variables. Generally, dense point clouds offer better surfaces and smoother displacement fields.

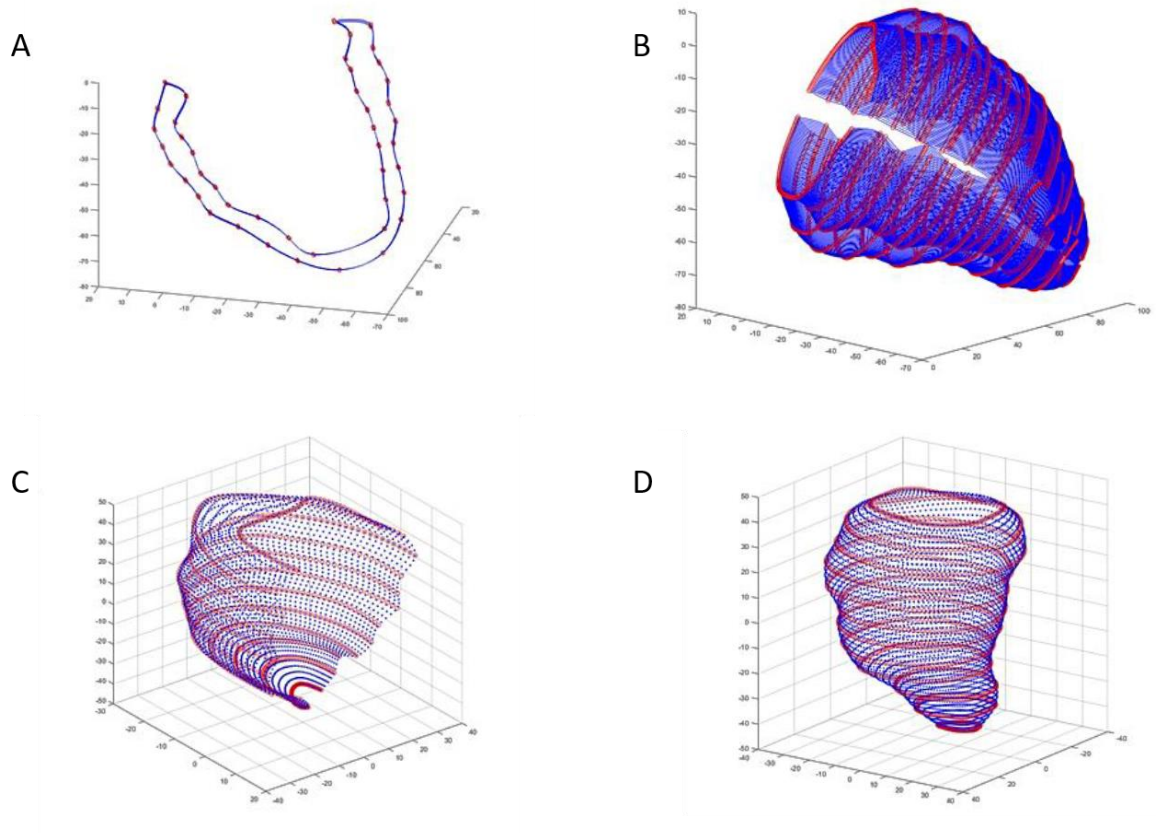

Figure 4. Example of stitching/joining scheme for (A, B) SAX point clouds and (C, D) combined 4CH, 2CH point clouds. Red corresponds to original sampled points and blue corresponds to interpolated points.

Meshing

The up sampling described above satisfies the purpose of generating smoother surfaces for enhanced displacement field interpolation. However, a continued presence of gaps or holes in the 3D ROI can be an obstacle to creating a surface representation of the LV. We thus developed in-house a customized automatic method to stitch/join user segmentation data, and to create the desired closed surface (Fig. 2D), with the added feature of controlling our resolution/point-density via user defined variables. Our method takes advantage of experienced-user input during segmentation and allows true morphological features to emerge within our 3D representation. In particular, after a new set of points is retrieved (Fig. 2B), we proceed to generate an initial surface triangulation using the boundary fitting method MATLAB, which is similar to the convex hull method (*MATLAB ® Mathematics R2020a*, 1984), but further allows the surface to shrink towards the interior of the hull to envelope all the points (*MATLAB ® Mathematics R2020a*, 1984). Subsequently, the surface is resampled, and a volume mesh is created using the iso2mesh utilities (Fang and Boas, 2009) which are based on Delaunay tetrahedralization of a closed surface. With our new set of nodes and their tetrahedral connectivity list, we obtain a complete volumetric representation of the LV (Fig. 2E) It is important to note that in case a surface mesh is already available, for example from an

external segmentation process, one only needs to align the surface mesh to the CMR image set and construct a volume mesh from the surface representation using the same utilities in the iso2mesh toolbox.

Displacement Field Interpolation

Given the up-sampled and reconstructed versions of the point clouds, it is necessary to interpolate the displacement fields at arbitrary locations over time and space. Here, we rely on the scattered interpolant method (Amidror, 2002) to compute interpolating functions for three axes of motion (X, Y, Z) by using function values from both the short axis tracked point cloud and the reconstructed long axis point cloud (Fig. 3A, B). The scattered interpolant relies on first constructing a Delaunay triangulation of the original sampled points. Next, any new query point is projected onto the convex hull of the sampled area, and the function value can be calculated using natural spline, linear or nearest neighbour interpolation options. When the query point lies inside the convex hull, the function value is interpolated, otherwise it is extrapolated using only the linear or nearest neighbour options. Finally, we can use the interpolants to compute displacement vectors at each time frame (Fig. 3C). In particular, we select the Z component of the displacements at a point to be exclusively represented by the interpolated values that come from the long axis view, given that we do not track long axis motion in short axis views, while we represent the X and Y components of displacement by a time-dependent weighted combination of long (4CH, 2CH) and short axis (SAX) views (Fig. 3D). The weights W influence the final displacements u, v in the X and Y directions at a point, depending on how much the given point has moved along the longitudinal direction $w_l$at a given time frame. W favours displacements obtained from the long axis u_l, v_lviews at times of large longitudinal deformation only, according to the formula,

$$W = \frac{w_l - w_{l,min}}{w_{l,max} - w_{l,min}} \quad (4)$$

$$u = (1 - W) * u_{cs} + W * u_l \quad (5)$$

$$v = (1 - W) * v_{cs} + W * v_l \quad (6)$$

Finally, with the obtained point (nodal) displacements, we compute the Greene-Lagrange strain E (Eq. 3) for each tetrahedral element via the deformation gradient (F) (Amini and Prince, 2001). The assembly of the required matrix calculations can be derived by standard finite element mapping (McGinty, 1986).

$$E = \frac{1}{2}(F^T F - I) \quad (7)$$

Validation and Analysis

For validation of our procedure, we focus on LV strain estimation on SSFP images. We here select the three benchmark results that were produced on such images in the STACOM 2011 challenge (Tobon-Gomez et al., 2013). Furthermore, we compare with the IUCL results also

presented in STACOM 2011, which included a combined approach between 3DTag and SSFP. We begin by a qualitative assessment of the strain field maps for a single volunteer dataset. We inspect local morphology changes during peak systole and compare visually to patterns obtained by STACOM 2011 participants. We then discuss the effect of using different motion tracking approaches and imaging modalities on the distribution of deformation and strain. Quantitative analysis is then performed for peak strains. Peak mid-ventricular strains were averaged across all samples. Results obtained from our proposed procedure will be tagged in the results section of this paper as AUC_AHC when comparing to the results reported by challenge participants (as available) and to suitable clinical reference benchmarks (Moore et al., 2000; Tobon-Gomez et al., 2013; Yingchoncharoen et al., 2013). Note that literature characterizes for end-systole a positive radial strain, a negative circumferential strain, and a longitudinal strain (of lower absolute magnitude than the radial component) (Moore et al., 2000; Yingchoncharoen et al., 2013).

Results

We here present our results for our procedure as applied to the STACOM 2011 datasets of the LV, which offers a valuable benchmarking platform for myocardial deformation and tracking algorithms. STACOM 2011 publicly shared its organized datasets of high quality, as well as the clinical metrics that were quantified from those datasets by four of the research groups that had responded to the challenge, the datasets are available online via the Cardiac Atlas Project (Tobon-Gomez et al., 2013). Each participant proposed their own myocardial motion tracking solution for the LV based on cine SSFP, tagged MR and/or 3DUS modalities. Each human volunteer's dataset was selected from healthy volunteers within certain age limits (28 ± 5 years old) and body surface area ($1.8 \pm 0.2 m^2$), to reduce physiological variability (Tobon-Gomez et al., 2013).

Qualitative Findings

Strain Magnitude

At peak systole, the radial strain ranges from **-0.5** to **0.5**, but is predominantly positive (indicating wall thickening), with the larger values more-or-less evenly distributed along the anterior (right side, free wall) of the ventricle, and the lower values appearing towards the interior (left side, septal) region. Minimum radial contraction appears at the most basal region (held back by atrial and valvular structures) and apical region (with the least amount of muscle) **(Fig. 4)**. Our results for this particular dataset, are visually comparable to those of UPF and INRIA in terms of field strength and general distribution. Furthermore, the circumferential strain ranges from **-0.25** to **0.25**, and is predominantly negative (which indicates a shrinking LV chamber). Positive values, however, are visible at the most basal anterior parts, due to a loss in circularity in that plane at peak systole **(Fig. 5)**. Our circumferential strain patterns for this dataset, seem to align best with the results of INRIA. The dissimilarity between reported results can in good part be ascribed to the degree of smoothing of the morphologies constructed in 3D of the LV, which results in different tangential/circumferential directions computed at each point on the mesh, and in turn projecting different circumferential components. Clearly, the radial strains are less sensitive to this issue. The longitudinal strain correspondingly ranges from **-0.25** to **0.25** and is mostly negative over a large part of the LV, with positive values appearing at the most basal anterior parts. Again, our results are qualitatively in good

agreement with those of UPF and INRIA, **(Fig. 5).** Finally, in terms of the trends of strain over the cardiac cycle, we summarize the computed average mid-ventricular strains in **(Fig. 6A)**.

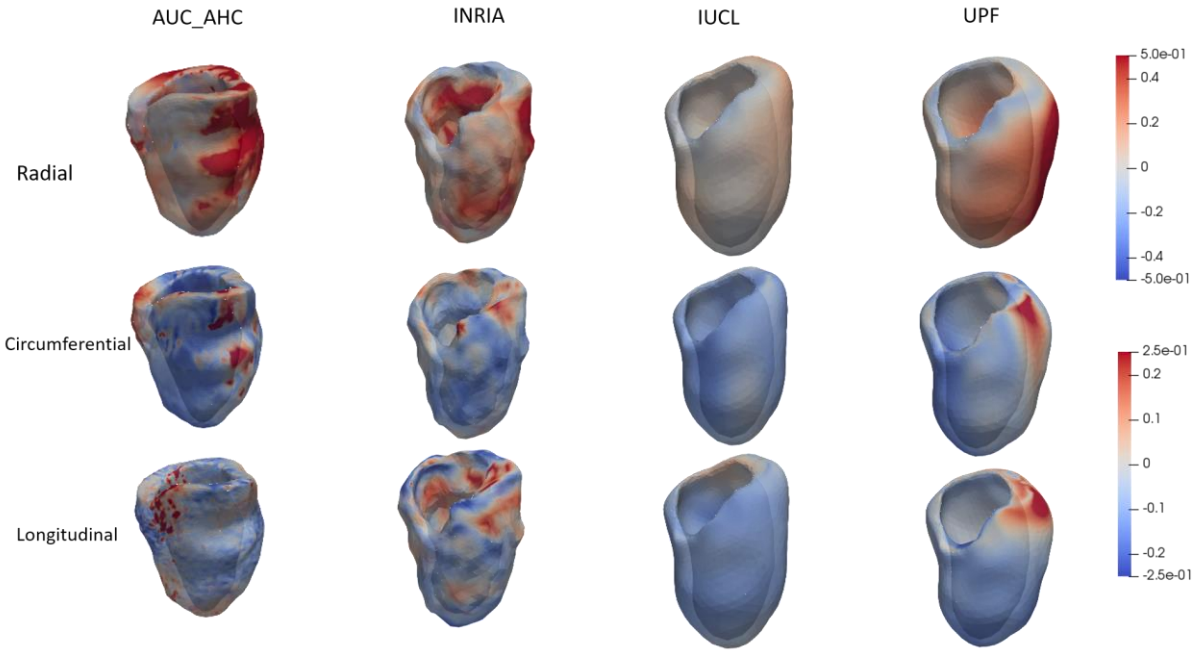

Figure 5. : Comparison of strain maps over volunteer 9 dataset between our proposed method and the results of the different participants on the same image modality. Strain ranges from –0.5-0.5 for radial, and –0.25-0.25 for longitudinal and circumferential components respectively.

Quantitative Findings

Peak Strain

The mean peak radial strain at the mid-ventricular level is estimated using our procedure to be (0.26 ± 0.07) vs. the (0.3 ± 0.08), (0.05 ± 0.04), (0.11 ± 0.1) reported by the challenge participants listed in the order shown in **(Fig. 6A)**. For the circumferential strain we estimate a mean peak value of (-0.14 ± 0.01) vs. the (-0.11 ± 0.02), (-0.1 ± 0.03), (-0.12 ± 0.2) reported by the challenge participants. Finally, the average peak mid-ventricular longitudinal strain is estimated to be (-0.12 ± 0.04) vs. the (-0.04 ± 0.01), (-0.13 ± 0.03), (-0.09 ± 0.2) reported by the challenge participants. With the IUCL approach we note a severe underestimation of radial strain, and a similarly severe underestimation of longitudinal strain by both the UPF and the INRIA procedures, obtained for the entire dataset. The underestimation is with respect to the reference clinical benchmarks at the mid-ventricular region, as reported in the literature, i.e. (0.44 ± 0.2), (-0.19 ± 0.04) and (0.15 ± 0.03) for radial, circumferential and longitudinal strain components respectively **(Fig. 6A)**, based on 3DTag imaging (Moore et al., 2000; Yingchoncharoen et al., 2013).

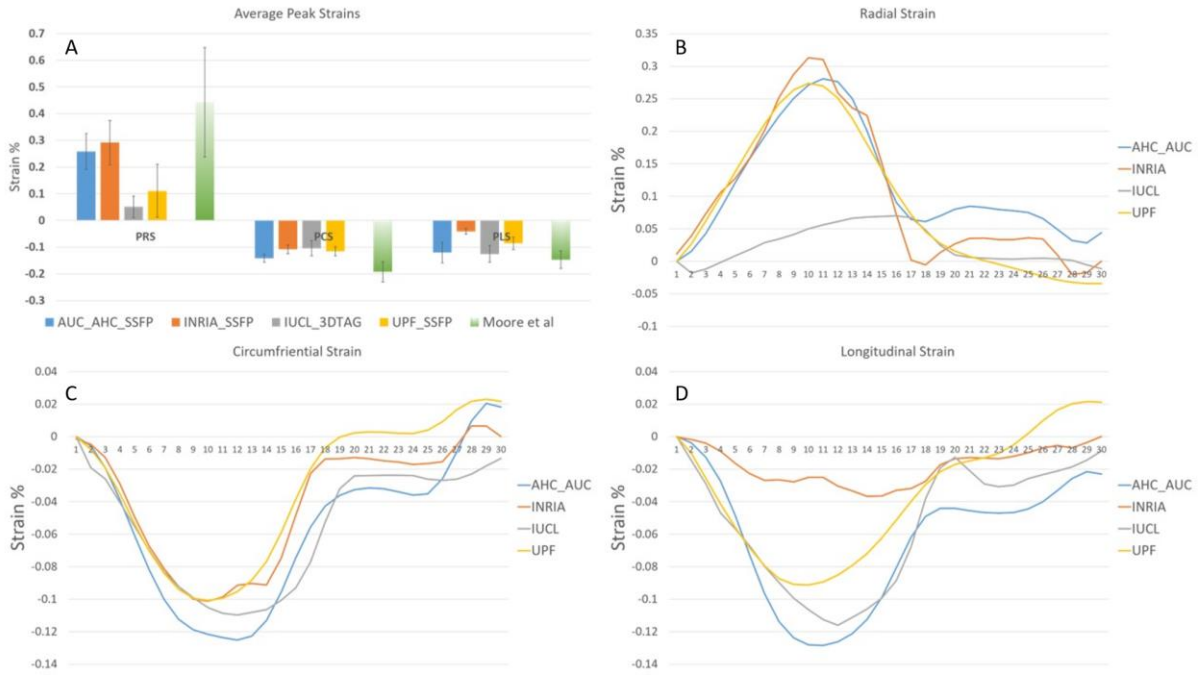

Figure 6. A) Bar chart with standard deviation error bars for average peak strains in the three major directions compared to other participants using same image modality and reference benchmark by Moore et al. B, C and D are strain curves in the three major directions for dataset of volunteer 9 compared to other participants in same image modality.

Landmark Tracking Error

Tracking error is defined as the Euclidean distance of the positions of landmarks using a proposed method and those observed by manual methods. For our proposed method that uses SSFP images only, we have a median tracking error of 4.9 ± 0.82 mm. The average error among participants using same image type is 4.8 mm, though it can be lower for other image types (Fig. 7).

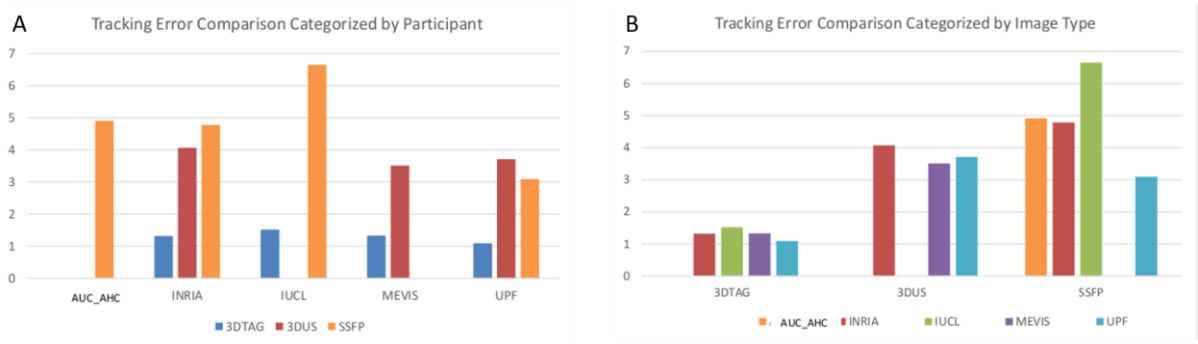

Figure 7. Median tracking bar chart error for comparing the approach with other participants. A) Categorized by participant, B) categorized by image modality.

Computational Speed

The run time of our codes per case are approximately 15 minutes, including the most time-consuming step of manual segmentation in the first timeframe for the different imaged

orientations, as well as the running of the strain analysis module on Segment. Here it is clear that we have a clear advantage over the codes used in the STACOM 2011 challenge (Fig. 8).

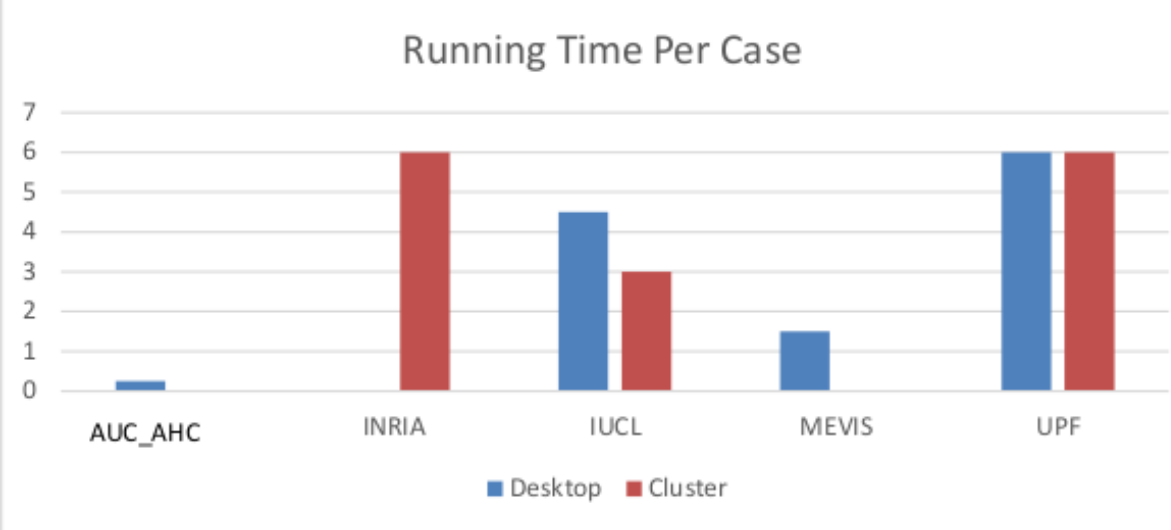

Figure 8. Average Running time in hours comparison per case with the different participants in the challenge categorized by desktop and cluster running configurations.

Discussion

In general, we note that our modelled strain maps are most like those reported by INRIA on the SSFP datasets, for the radial and circumferential components (**Fig. 5**). Also, clear improvement is offered by our procedure, with respect to the results reported in the challenge, in terms of the following important metrics. First, in in terms of components magnitude (Moore et al., 2000; Tobon-Gomez et al., 2013; Yingchoncharoen et al., 2013) in terms of being the method closest to reference values as well as higher sensitivity in capturing peak strain patterns in the different directions. Second, in terms of general curve smoothness (Duckett et al., 2012; Tobon-Gomez et al., 2013) which may indicate that our method is more robust to noisy acquisitions and myocardial tracking errors. Concerning our modelled strain magnitudes, as with all Challenge participants, we underestimate the peak values, with varying degrees for each component. Here, we compute a peak radial strain of (26 ± 6 %) (Fig. 7), consistent with challenge participants and with previous studies made on SSFP images (Duckett et al., 2012; Tobon-Gomez et al., 2013). We also have good agreement in circumferential strain (14 ± 1.4%) with the participants (Fig. 7), when focusing on the SSFP modality. Our approach however is the most capable among the approaches we here compare to reproduce clinically anticipated longitudinal strains (-12 ± 4%). It does so, without compromising the quality of its radial and circumferential estimates, and without resorting to other imaging modalities. Finally, we remark that a source of underestimation affecting strain estimates in all the approaches we here compared is the lack of enforcement of incompressibility on the myocardium (Amini and Prince, 2001; Duckett et al., 2012; Rueckert and Aljabar, 2010; Wang and Amini, 2012). As the LV walls thicken between diastole and systole within a cardiac cycle, with an underestimated longitudinal motion, an enlarged myocardial volume will result, which violates incompressibility. All computed strain components are thus calculated with respect to enlarged tetrahedral elements, which for the same displacements will return underestimated strains. In our proposed approach the tracking error seems generally higher than that reported for the other image modalities (**Fig. 7**A). However, we note that it is well within the range reported specifically for methods based on SSFP images (**Fig. 7**B), as were used in our research. This larger error is

partly explained by the fact that our manually observed landmarks were extracted from 3DTag images only (Tobon-Gomez et al., 2013). Therefore, inherent spatial misalignment between the two image sets may induce a slight drift effect that influences the error for SSFP images in general. More importantly, as the error in position appears to be predominantly along the long axis coordinate (Z-axis), we believe that SSFP images tend to underestimate longitudinal motions of the LV, consistent with the findings of previous experiments by IUCL (Duckett et al., 2012). Our method is computationally more efficient than those showcased in the STACOM 2011 challenge **(Fig. 8)**. This of course may be in part due to the faster hardware that became available since the publication of the challenge (Tobon-Gomez et al., 2013). However, our reliance on two-dimensional registration (Morais et al., 2017), compared to the three-dimensional registration shared by most of the participants seems to be a key factor in our speed-up. This may be explained by our reliance on 2D+t registration method (Heyde et al., 2013) adopted in **Segment** which in terms of the optimization loops drops the complexity of the problem by one spatial dimension which naturally reduces the computational complexity of determining optimal control point displacements (Rueckert and Aljabar, 2010) in two dimensions vs three dimensions (Rueckert and Aljabar, 2010; Schwarz, 2007), this is complemented by introducing the 3rd dimension motion component via our low cost scattered interpolation scheme post-registration and weighing scheme (Fig. 3) to modulate influence of different displacement fields. Also, we generated significantly coarser meshes to obtain comparable results to those of the participants, which while providing reasonable accuracy, may produce erroneous strain values if a regional assessment is adopted due to shape discontinuities (i.e. divide the lv in to discrete segments and calculate an average strain), this can be remedied by adjusting the density and resolution of the meshing process by controlling the element size, no. of elements and specify a minimum diameter for hole filling as described here (Fang and Boas, 2009). Moreover, our proposed method includes concurrent interpolation for each timeframe independently**,** which drastically improved our computational cost in the large batch studies that were configured to run on a cluster environment (Fig. 8), this was accomplished by exploiting the inherent concurrency of the problem, in that spatial interpolation can be performed at each frame independently. We remark here that our most time-consuming step remains in the initial segmentation. It should be noted that more rigorous complexity analysis of the different steps used in our framework is needed to accurately assess performance as being independent on software platform or hardware being used.

Conclusions

Motion analysis of a beating heart has important clinical implications in the characterization of heart disease. It is associated with structural and functional changes with respect to normal conditions. Rapid advancements to imaging technologies, image processing, image registration and computer visualization afford us an opportunity for patient-specific quantification of normal and abnormal patterns of deformation. These advancements promise a better understanding of the underlying cardiac conditions to support standard clinical practices, such as diagnosis, pre-operative surgery planning, and post-operative assessment. In this work we have set out to develop a computational framework that generates a four-dimensional model of the LV, which incorporates information on LV structure and deformation through geometric approaches that interpolate between a set of 2D displacements, using 3D spatial interpolation. We developed an end-to-end procedure for motion analysis by generating our 3D geometric representation from the 2D data, and by creating a volumetric mesh representation for the myocardium, which allows a more accurate representation of myocardial deformation (via finite element approximation functions that capture through-thickness strain components). Our procedure is computationally inexpensive and fully automated, except for the initial

segmentation step. Our procedure also does not rely on multi-modal datasets, special imaging methods or additional image annotation, only the commonest imaging modality with standard LV contouring in the first time frame based on tracking results provided by one of the few clinically used software for LV function assessment on untagged CMR images, to produce fast quality predictions of strain (radial, circumferential and longitudinal), which is a key feature sought by our procedure for broad clinical and patient-specific application.

Data Availability

The unprocessed data sets used in this research are publicly available on the cardiac atlas project as part of the STACOM 2011 challenge dataset. The processed vtk files which contain the resulting data from applying the framework which was used to support the findings of this study are available from the corresponding author upon request.

Conflicts of Interest

The authors declare that they have no conflict of interest.

Funding Statement

This work is based on the master thesis of the first author Mohamed Abdelkhalek, published in university archives on May 2019 (Abdelkhalek et al., 2019).

Supplementary Materials

1) Video animation of original tracked points from software and then, of final interpolated mesh as it deforms due to influence of combined displacement from the multiple views.

References

Abdelkhalek, M., Aguib, H., Moustafa, M., Elkhodary, K., 2019. Semi-automatic spatio-temporal reconstruction of the left ventricle from CMR. The American University in Cairo.

Amidror, I., 2002. Scattered data interpolation methods for electronic imaging systems: a survey. J. Electron. Imaging. https://doi.org/10.1117/1.1455013

Amini, A.A., Prince, J.L. (Eds.), 2001. Measurement of Cardiac Deformations from MRI: Physical and Mathematical Models, Computational Imaging and Vision. Springer Netherlands, Dordrecht. https://doi.org/10.1007/978-94-015-1265-7

Baillargeon, B., Rebelo, N., Fox, D.D., Taylor, R.L., Kuhl, E., 2014. The living heart project: A robust and integrative simulator for human heart function. Eur. J. Mech. A/Solids 48, 38–47. https://doi.org/10.1016/j.euromechsol.2014.04.001

De Santis, G., Verhegghe, B., Canè, F., Segers, P., Bertrand, P.B., De Beule, M., Van der Geest, R.J., 2018. From 4D Medical Images (CT, MRI, and Ultrasound) to 4D Structured Mesh Models of the Left

Ventricular Endocardium for Patient-Specific Simulations. Biomed Res. Int. 2018, 1–14. https://doi.org/10.1155/2018/7030718
Duckett, S., Edwards, P.J., Wenzhe Shi, Rhode, K.S., Xiahai Zhuang, Ourselin, S., Razavi, R.S., Haiyan Wang, KaiPin Tung, Tobon-Gomez, C., Rueckert, D., Luong, D.V.N., 2012. A Comprehensive Cardiac Motion Estimation Framework Using Both Untagged and 3-D Tagged MR Images Based on Nonrigid Registration. IEEE Trans. Med. Imaging 31, 1263–1275. https://doi.org/10.1109/tmi.2012.2188104
Fang, Q., Boas, D.A., 2009. Tetrahedral mesh generation from volumetric binary and grayscale images, in: Proceedings - 2009 IEEE International Symposium on Biomedical Imaging: From Nano to Macro, ISBI 2009. https://doi.org/10.1109/ISBI.2009.5193259
Ginat, D.T., Fong, M.W., Tuttle, D.J., Hobbs, S.K., Vyas, R.C., 2011. Cardiac imaging: Part 1, MR pulse sequences, imaging planes, and basic anatomy. Am. J. Roentgenol. https://doi.org/10.2214/AJR.10.7231
Ginnis, A.I., Kostas, K. V., Kaklis, P.D., 2017. Construction of smooth branching surfaces using T-splines. CAD Comput. Aided Des. https://doi.org/10.1016/j.cad.2017.06.001
Gray, R.A., Pathmanathan, P., 2018. Patient-specific cardiovascular computational modeling: Diversity of personalization and challenges. J. Cardiovasc. Transl. Res. 11, 80–88. https://doi.org/10.1007/s12265-018-9792-2
Hergan, K., Schuster, A., Frühwald, J., Mair, M., Burger, R., Töpker, M., 2008. Comparison of left and right ventricular volume measurement using the Simpson's method and the area length method. Eur. J. Radiol. 65, 270–278. https://doi.org/10.1016/j.ejrad.2007.03.031
Heyde, B., Member, Student, Jasaityte, R., Barbosa, D., Robesyn, V., Bouchez, S., Wouters, P., Maes, F., Member, Senior, Claus, P., Jan, D., 2013. for 2-D Myocardial Motion Estimation : A Direct Comparison In Vivo. IEEE Trans. image Process. 32, 449–459.
Lee, E.T.Y., 1989. Choosing nodes in parametric curve interpolation. Comput. Des. https://doi.org/10.1016/0010-4485(89)90003-1
MATLAB ® Mathematics R2020a, 1984.
McGinty, 1986. Finite elements. [WWW Document]. URL https://www.continuummechanics.org/finiteelementmapping.html (accessed 5.12.20).
Medvedofsky, D., Maffessanti, F., Weinert, L., Tehrani, D.M., Narang, A., Addetia, K., Mediratta, A., Besser, S.A., Maor, E., Patel, A.R., Spencer, K.T., Mor-Avi, V., Lang, R.M., 2018. 2D and 3D Echocardiography-Derived Indices of Left Ventricular Function and Shape: Relationship With Mortality. JACC Cardiovasc. Imaging. https://doi.org/10.1016/j.jcmg.2017.08.023
Moore, C.C., Lugo-Olivieri, C.H., McVeigh, E.R., Zerhouni, E.A., 2000. Three-dimensional systolic strain patterns in the normal human left ventricle: Characterization with tagged MR imaging. Radiology. https://doi.org/10.1148/radiology.214.2.r00fe17453
Morais, P., Heyde, B., Barbosa, D., 2013. Functional Imaging and Modeling of the Heart 7945. https://doi.org/10.1007/978-3-642-38899-6
Morais, P., Marchi, A., Bogaert, J.A., Dresselaers, T., Heyde, B., D'Hooge, J., Bogaert, J., 2017. Cardiovascular magnetic resonance myocardial feature tracking using a non-rigid, elastic image registration algorithm: assessment of variability in a real-life clinical setting. J. Cardiovasc. Magn. Reson. 19, 1–13. https://doi.org/10.1186/s12968-017-0333-y
Rueckert, D., Aljabar, P., 2010. Nonrigid registration of medical images: Theory, methods, and applications. IEEE Signal Process. Mag. 27, 113–119. https://doi.org/10.1109/MSP.2010.936850
Schulz-Menger, J., Bluemke, D.A., Bremerich, J., Flamm, S.D., Fogel, M.A., Friedrich, M.G., Kim, R.J., Von Knobelsdorff-Brenkenhoff, F., Kramer, C.M., Pennell, D.J., Plein, S., Nagel, E., 2020. Standardized image interpretation and post-processing in cardiovascular magnetic resonance - 2020 update: Society for Cardiovascular Magnetic Resonance (SCMR): Board of Trustees Task Force on Standardized Post-Processing. J. Cardiovasc. Magn. Reson. https://doi.org/10.1186/s12968-020-00610-6
Schwarz, L.A., 2007. Non-rigid registration using free-form deformations. Ph. D. Diss. Dept. Comput. Sci., Tech. Univ. Munchen.
Tobon-Gomez, C., De Craene, M., McLeod, K., Tautz, L., Shi, W., Hennemuth, A., Prakosa, A., Wang, H., Carr-White, G., Kapetanakis, S., Lutz, A., Rasche, V., Schaeffter, T., Butakoff, C., Friman, O., Mansi, T., Sermesant, M., Zhuang, X., Ourselin, S., Peitgen, H.O., Pennec, X., Razavi, R., Rueckert, D., Frangi, A.F., Rhode, K.S., 2013. Benchmarking framework for myocardial tracking and deformation algorithms: An open access database. Med. Image Anal. 17, 632–648. https://doi.org/10.1016/j.media.2013.03.008
Wang, H., Amini, A.A., 2012. Cardiac motion and deformation recovery from MRI: A review. IEEE Trans. Med. Imaging 31, 487–503. https://doi.org/10.1109/TMI.2011.2171706
Werys, K., Blaszczyk, L., Kubik, A., Marczak, M., Bogorodzki, P., 2015. Displacement field calculation from CINE MRI using non-rigid image registration. Proc. 2015 IEEE 8th Int. Conf. Intell. Data Acquis. Adv. Comput. Syst. Technol. Appl. IDAACS 2015 2, 672–675. https://doi.org/10.1109/IDAACS.2015.7341388
Yingchoncharoen, T., Agarwal, S., Popović, Z.B., Marwick, T.H., 2013. Normal ranges of left ventricular strain:

A meta-analysis. J. Am. Soc. Echocardiogr. https://doi.org/10.1016/j.echo.2012.10.008